Article

Enhanced Electrochemical Performance of Lithium Iron Phosphate Cathodes Using Plasma-Assisted Reduced Graphene Oxide Additives for Lithium-Ion Batteries

Suk Jekal [†], Chan-Gyo Kim [†], Jiwon Kim, Ha-Yeong Kim, Yeon-Ryong Chu, Yoon-Ho Ra, Zambaga Otgonbayar * and Chang-Min Yoon *[iD]

Department of Chemical and Biological Engineering, Hanbat National University, Daejeon 34158, Republic of Korea
* Correspondence: zambaga@hanbat.ac.kr (Z.O.); cmyoon4321@hanbat.ac.kr (C.-M.Y.);
  Tel.: +82-42-821-1528 (C.-M.Y.); Fax: +82-42-821-1593 (C.-M.Y.)
[†] These authors contributed equally to this work.

Abstract: One-dimensional lithium-ion transport channels in lithium iron phosphate (LFP) used as a cathode in lithium-ion batteries (LIBs) result in low electrical conductivity and reduced electrochemical performance. To overcome this limitation, three-dimensional plasma-treated reduced graphene oxide (rGO) was synthesized in this study and used as an additive for LFP in LIB cathodes. Graphene oxide was synthesized using Hummers' method, followed by mixing with LFP, lyophilization, and plasma treatment to obtain LFP@rGO. The plasma treatment achieved the highest degree of reduction and porosity in rGO, creating ion transfer channels. The structure of LFP@rGO was verified through scanning electron microscopy (SEM) analysis, which demonstrated that incorporating 10.0 wt% of rGO into LFP resulted in successful coverage by the rGO layer, forming LFP@rGO-10. In half-cell tests, LFP@rGO-10 exhibited a specific capacity of 142.7 mAh g^{-1} at the 1.0 C-rate, which is higher than that of LFP. The full-cell exhibited 86.8% capacity retention after 200 cycles, demonstrating the effectiveness of rGO in enhancing the performance of LFP as an LIB cathode mAterial. The outstanding efficiency and performance of the LFP@rGO-10//graphite cell highlight the promising potential of rGO-modified LFP as a cathode mAterial for high-performance LIBs, providing both increased capacity and stability.

Keywords: high energy density; lithium iron phosphate; reduced graphene oxide; lyophilization; plasma treatment

1. Introduction

The rapid expansion of various industries has led to an increase in the demand for electrical energy, underscoring the importance of highly efficient energy-storage systems [1,2]. Lithium-ion batteries (LIBs) have gained considerable attention for use in a wide range of applications, including electrical devices, electric vehicles, and portable gadgets, to fulfill this growing requirement [3–7].

LIBs are preferred because of their advantages, such as high energy density, long cycle life, and stable performance. The LIBs include a cathode, an anode, a separator, and an electrolyte [8,9]. These components work together to store and release electrical energy through electrochemical reactions, specifically oxidation/reduction (redox) processes, which occur between the cathode and anode [10]. The electrochemical performance of an LIB is affected by the active mAterial used in the electrodes [11]; these mAterials directly participate in redox reactions and determine the energy storage capacity of the battery, efficiency, and rate of energy conversion [12,13]. Cathode mAterials can significantly affect the overall performance and longevity of LIBs [14]. mAterials used to prepare LIB cathodes include lithium nickel cobalt aluminum oxide (NCA), lithium nickel mAnganese cobalt

oxide (NMC), and lithium cobalt oxide (LCO) [15–17]. Each mAterial is selected for specific applications based on its distinct properties. Specifically, LCO is widely used in portable devices due to its high energy density, whereas NMC and NCA are preferred for electric vehicles because of their superior power delivery and energy efficiency [18–20]. Despite their widespread use, NMC and NCA cathodes have some drawbacks, which include high production costs, environmental toxicity, and limited resource availability for large-scale mAnufacturing [21–23]. To overcome these limitations, existing research focused on lithium iron phosphate (LFP) as a promising cathode mAterial for next-generation LIBs. The olivine structure of LFP provides several benefits, such as high thermal stability, low cost, nontoxicity, and the abundant availability of raw mAterials [24–26]. The olivine structure of LFP is characterized by oxygen atoms arranged in a distorted hexagonal close-packed structure, which creates a stable crystal lattice that facilitates lithium-ion movement along one-dimensional (1D) channels [27]. This structural stability enables LFP to mAintain its integrity during repeated charge/discharge cycles [28]; however, the 1D lithium-ion transport channels limit ion mobility and restrict electron transport to Fe–O–Fe pathways, resulting in low electrical conductivity and reduced electrochemical performance, especially at high charge/discharge rates (high C-rate regions) [29].

Several strategies have been explored to overcome these limitations, such as reducing LFP particle size, doping with other elements to optimize the lattice, and coating with conductive carbon mAterials like CNTs, amorphous carbon, carbon black, and graphene oxide (GO) [30–33]. It is known that adding carbon mAterials to LFP to prepare the LIB cathode mAterial results in improved electrochemical performance compared to using LFP alone as a cathode mAterial. This is attributed to the high conductivity of carbon mAterials, which form a conductive network to enhance electron and Li-ion transfer, improve the structural integrity of the electrode mAterial, and create a barrier layer to prevent side reactions that produce unwanted byproducts, leading to a high charge/discharge rate and capacity. However, not all carbon mAterials are compatible with LFP. One-dimensional CNTs form continuous conductive networks, minimize electrode degradation by reducing mechanical strain during the charge/discharge cycle, and bridge the gaps between LFP particles, thus reducing internal resistance and enhancing electron and ion mobility, but achieving uniform dispersion is challenging [34]. Amorphous carbon improves stability and reduces volume changes in LFP during recycling tests but increases weight, lowering the energy density [35]. Furthermore, carbon black, one of the cost-effective conductive additives for LFP, improved the conductivity of the cathode mAterial but has limited effectiveness due to its lower surface area and non-continuous structure [36].

Among these conductive mAterials, graphene oxide has emerged as an exceptional mAterial for enhancing electrode performance in energy storage devices [37]. The two-dimensional (2D) sheet-like structure of graphene oxide, composed of carbon atoms (C) arranged in a single layer, provides high electrical conductivity, large surface area, and excellent chemical stability. The C–C π-bonds in graphene form a conductive band, enabling rapid electron transport across the graphene layers [38–40]. However, graphene has limitations in achieving the highest electrochemical performance caused by volumetric changes and hindered Li-ion movement [41]. The drawbacks of graphene oxide can be addressed by modifying its structure to produce reduced graphene oxide (rGO), which exhibits improved electrical conductivity and can be used as an active mAterial in energy-storage devices. However, high-temperature thermal and chemical treatments are required to reduce graphene oxide to form rGO, which causes rGO sheets to restack owing to van der Waals forces [42]. This restacking reduces the specific surface area and, when combined with LFP, diminishes the overall electrochemical performance of the composite, thereby affecting the efficiency of the energy storage device [43]. One strategy to prevent restacking and hindered Li$^+$ movement in GO is to form a three-dimensional (3D) structure. Plasma-assisted photothermal reduction has been proposed as an alternative approach to mitigate rGO sheet restacking and to achieve a high degree of reduction [44]. Plasma comprises a mixture of free-moving charged particles (ions and electrons) and is generated by ex-

posing specific gases to high energies, such as heat or electromagnetic fields, to ionize gas atoms [45]. Plasma-assisted reduction offers advantages such as short processing times and non-toxic environments. During the reduction process, the plasma generates high pressure between the rGO sheets, releasing gases such as CO_2 and H_2O that prevent restacking and promote the formation of pores on the rGO surface, thereby increasing its surface area [46]. The dimensions of rGO can be expanded further by lyophilization (freeze drying) before plasma reduction, which positively influences the lithium-ion transfer properties by creating a more open structure [47].

In this study, rGO was added as a conductive agent to enhance the electrochemical performance of LFP-based cathodes in LIBs. The GO content was controlled at 5.0, 10.0, and 15.0 wt% before being reduced to rGO. Using lyophilization and plasma-assisted reduction, the LFP was coated with rGO sheets, producing LFP@rGO-5, LFP@rGO-10, and LFP@rGO-15. The compositions, structures, and morphologies of the LFP@rGO composites were analyzed to confirm successful fabrication and electrochemical studies were conducted on various LFP@rGO-based electrodes. The LFP@rGO-10 electrode showed significantly higher specific capacity than the LFP-based electrode, attributed to optimal rGO mixing, which enhanced conductivity and improved ion transfer. In LIB applications, the full-cell with LFP@rGO-10 as the cathode and graphite as the anode displayed excellent electrochemical performance, including long-term cyclability. Therefore, the rGO synthesized in this study shows promise as an additive for improving LFP in LIBs.

2. Materials and Methods

2.1. Materials

Graphite (200 mesh, ≤74 µm), 1-methyl-2-pyrrolidinone (NMP), polyvinylidene fluoride (PVDF, M_w = 534,000), ethylene carbonate (EC), and ethyl methyl carbonate (EMC) were obtained from Merck Co. (Darmstadt, Germany). Sulfuric acid (H_2SO_4, 99.5%), hydrogen chloride (HCl, 35.0%), sodium nitrate ($NaNO_3$, 99.0%), potassium mAnganate ($KMnO_4$, 99.3%), hydrogen peroxide (H_2O_2, 30.0%), and sodium nitrate ($NaNO_3$, 99.0%) were purchased from Samchun Chemical Co. (Pyeongtaek, Republic of Korea). Lithium iron phosphate (LFP; $LiFePO_4$, 99.5%) and lithium hexafluorophosphate ($LiPF_6$) were obtained from Tokyo Chemical Industry Co. (Tokyo, Japan). Carbon black was acquired from Thermo Fisher Scientific (Waltham, mA, USA). The cathode current collector, aluminum (Al) foil, was sourced from Sam-A Aluminum (Pyeongtaek, Republic of Korea), while the anode current collector, 20 µm copper (Cu) foil, was purchased from Iljin mAterials (Iksan, Republic of Korea). All chemical reagents and mAterials were used as received without further treatment.

2.2. Synthesis of Plasma-Assisted LFP/Reduced GO Composite (LFP@rGO)

Graphene oxide (GO) was synthesized using a modified Hummers' method [48], and the detailed experimental procedure is described in our previous article [49]. The synthesis of the plasma-assisted LFP/reduced GO composite (LFP@rGO) began with the preparation of the GO solution. In detail, the GO (0.25 g) was dispersed in DI water and sonicated for 1 h. LFP was then added to the GO solution with continuous stirring. The concentration of GO was controlled at 5.0–15.0 wt% to obtain the optimum value of GO to LFP (LFP@GO). Prior to plasma treatment, the solution was freeze-dried for 48 h to remove water molecules using a freeze-dryer (TFD 8501, Ilshin Bio Base, Seoul, Republic of Korea). Subsequently, plasma treatment under atmospheric conditions was performed to obtain an LFP@rGO using plasma instrument (MyPL-100P, APP Co., Ltd., Hwaseong, Republic of Korea). In the experiment, the sample was placed vertically and exposed to the plasma curtain. For the plasma treatment, the power was set at 150 W, with a gas flow of oxygen (20 sccm) and argon (4.0 L min^{-1}) to generate a plasma curtain using radio frequency (13.56 MHz). The resulting LFP@rGO composite was then stored in a vacuum oven overnight to remove moisture. For comparison purposes, carbon black-coated LFP (LFP@C-10) was synthesized

by mixing LFP (1.8 g), and carbon black (0.2 g) was ground using mortar and pestle for 2 h. The mixed powder was then heated in a tube furnace at 800 °C for 2 h.

2.3. Morphology and Molecule Structure Analysis

The surface of the LFP@rGO composites was analyzed using scanning electron microscopy (SEM, S-4800, Hitachi, Tokyo, Japan). The chemical compositions of the samples were measured using an energy-dispersive X-ray spectrometer (EDS, EX-250, HORIBA Co., Kyoto, Japan) installed in the SEM. The crystallinity of the samples was examined using X-ray diffraction (XRD, D8 Advance, Bruker Co., Billerica, mA, USA). The molecular structure of the samples was analyzed by Raman spectroscopy (QE Pro, Ocean Optics Inc., Largo, FL, USA) and Fourier-transform infrared (FT-IR, Nicolet iS10, Thermo Fisher Scientific, Waltham, mA, USA).

2.4. Electrochemical Measurements

The electrochemical performance of the prepared samples was evaluated using 2032 coin-type cells. For the half-cell, lithium (Li) metal was employed as both the reference and counter electrodes. To fabricate the cathode, a slurry was prepared by dissolving the active mAterial (LFP, LFP@rGO, or LFP@C-10), conductive mAterial (carbon black), and binder (PVDF) in a mAss ratio of 8:1:1, and dissolving the mixture in NMP solvent. Then, the slurry was coated on an Al-foil with a thickness of 180 μm using a doctor blade, followed by drying in a vacuum oven (110 °C) for 5 h to remove the residual. To prepare the coin-cell electrode, the as-prepared Al-foil was pressed and punched into circular disks with a diameter of 14 mm. The electrolyte of 1.0 M $LiPF_6$ in EC and EMC was mixed in a volume ratio of 3:7. For full-cell assembly, the anode was prepared by mixing graphite, conductive mAterial, and binder in a weight ratio of 9:0.5:0.5 to form the slurry, which was then coated onto copper (Cu) foil using the same method. The electrode assembly was performed in a glove box (MOtek, Daejeon, Republic of Korea) filled with high-purity argon gas (99.9995%). The galvanostatic charge/discharge (GCD) between 2.50 and 4.30 V vs. Li/Li$^+$ with different current rates (C-rates) (1.0 C: 170 mAh g^{-1}) was measured using potentiostat/galvanostat instrument (WBCS 3000, WonATech, Seoul, Republic of Korea). Cyclic voltammetry (CV) and electrochemical impedance spectroscopy (EIS) measurements were performed in the frequency range of 100 kHz to 5 mHz using an electrochemical workstation (Zive SP1, WonATech, Seoul, Republic of Korea).

3. Results and Discussion

3.1. Fabrication of the LFP@rGO Composite

Figure 1 shows SEM micrographs highlighting the morphology and surface interactions of LFP and its composites with varying amounts of rGO. The SEM micrographs of GO and rGO are presented in Figure S1. A porous web structure formed in GO during the freeze-drying process. Following plasma treatment, a porous structure was formed on the GO sheet, thereby validating the ion transfer channel. The micrograph in Figure 1a shows LFP, characterized by densely packed particles with irregular shapes [50,51]. These particles exhibited typical LFP features, including a crystalline nature, without any coating or surface modification, as evidenced by their homogeneous appearance. In contrast, Figure 1b shows LFP@rGO-5, where a thin rGO layer partially covers the LFP particles. The yellow dotted circles highlight the regions of initial rGO incorporation, suggesting minimal yet sufficient interactions to begin altering the LFP surface characteristics. The rGO layer was thin and dispersed, indicating the formation of a conductive network that enhanced the electronic conductivity of the composite. This interaction becomes more observable with an increase in the rGO content (LFP@rGO-10) (Figure 1c). The SEM micrograph shows more extensive rGO coverage, with more uniformly distributed sheets that are closely associated with the LFP particles, thereby forming a continuous conductive network. This suggests enhanced electronic properties, as rGO creates a conductive path for electron transport between the LFP particles. Figure 1d, which shows the micrograph for LFP@rGO-15, reveals a

significant increase in rGO coverage. The LFP particles are almost entirely encapsulated by rGO, forming a densely interconnected network. The yellow dotted circles highlight comprehensive rGO coverage, indicating a robust conductive mAtrix around the LFP particles at this concentration. The extensive rGO coverage is anticipated to significantly improve electrical conductivity and performance, mAking the composite more suitable for LIB applications. The EDS elemental analysis confirmed these observations, verifying the presence and distribution of key elements (Table 1). In the LFP sample, EDS showed peaks corresponding to iron (Fe), phosphorus (P), and oxygen (O), which is consistent with the composition of LFP [52]. Additional carbon (C) peaks in the LFP/rGO samples confirmed successful rGO incorporation, with the carbon peak intensity increasing from LFP@rGO-5 to LFP@rGO-15, thereby reflecting the higher rGO content. SEM micrographs and EDS analysis demonstrated the structural change and enhanced interaction between LFP and rGO with an increase in rGO content [53]. These interactions play an important role in enhancing the electronic properties of the sample, mAking the composites promising candidates for high-performance energy storage applications.
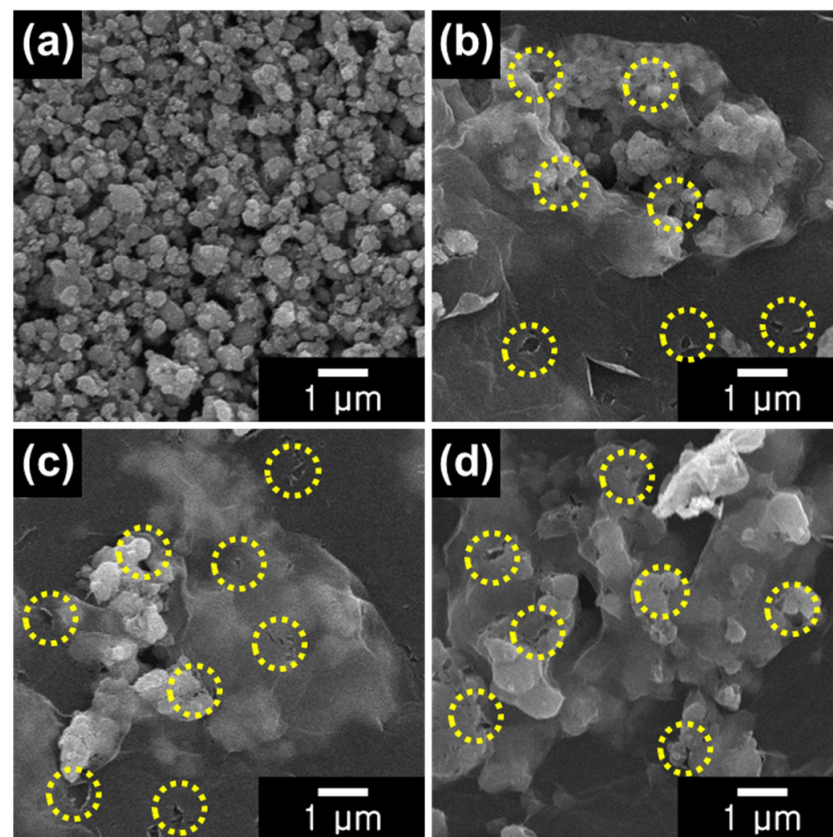

Figure 1. SEM micrographs of the (**a**) LFP, (**b**) LFP@rGO-5, (**c**) LFP@rGO-10, and (**d**) LFP@rGO-15.

Table 1. Elemental compositions of rGO-coated LFP with various concentrations [a].

Sample	Element (Atomic %)				
	Li	**Fe**	**P**	**O**	**C**
LFP	-	34.0	17.0	49.0	-
LFP@rGO-5	-	32.5	16.1	46.7	4.7
LFP@rGO-10	-	30.7	14.9	44.5	9.9
LFP@rGO-15	-	28.9	13.1	43.4	14.6

[a] Elemental compositions of samples obtained by the EDS mode installed in SEM (beam current: 10.0 μA, accelerating voltage: 10.0 kV).

The SEM and EDS analyses indicated that increasing the rGO content to fabricate the LFP@rGO composites can significantly enhance their electronic properties. LFP particles exhibited a dense and uniform distribution without surface modifications; however, even minimal rGO introduction resulted in the formation of a thin dispersed layer, which formed a conductive network. The network became more noticeable and uniformly distributed with an increase in the rGO content, which improved the electron transport. At the highest rGO concentration, the LFP particles were encapsulated by rGO, forming a densely interconnected network that enhances electrical conductivity, mAking the LFP@rGO composites highly suitable for advanced energy-storage applications.

The XRD analysis examined the crystallinity of the LFP and its composites with varying amounts of rGO, designated as LFP@rGO-5, LFP@rGO-10, and LFP@rGO-15 (Figure 2). The distinct sharp XRD peaks detected in LFP indicated an orthorhombic olivine structure with the P_{nma} space group, confirming its high-purity crystalline phase with no secondary phases or impurities observed (PDF#81-1173) [54]. The composite mAterials, including LFP@rGO-5, LFP@rGO-10, and LFP@rGO-15 exhibited similar diffraction peaks corresponding to the LFP phase, indicating that the crystal structure of LFP remained stable and unaffected by rGO [55]. For LFP@rGO-10 and LFP@rGO-15, a noticeable reduction in the peak intensities is observed as the rGO content increases, attributed to the increased presence of rGO and the broad peak at 26°, relating to the (002) plane of graphitic carbon. The broadening of this peak or its partial overlap with LFP peaks suggests that the rGO sheets were well-dispersed around the LFP particles, forming an amorphous or semi-crystalline mAtrix that slightly reduced the overall crystallinity of the composite. In addition, the slight broadening of the diffraction peaks was observed in the LFP@rGO composites, particularly in LFP@rGO-15 [56]. This broadening can indicate a decrease in the LFP crystallite size because of the interaction between LFP and rGO during synthesis, where rGO can induce strain or defects in the LFP structure. Overall, the XRD analysis confirmed that the crystalline structure of LFP was mAintained across all samples despite the increasing presence of rGO. The slight reduction in peak intensity and broadening indicates successful rGO incorporation into LFP, enhancing the electrochemical performance of the composite by forming a conductive network without significantly disrupting the crystal structure, mAking these stable composites promising candidates for advanced LIB applications.
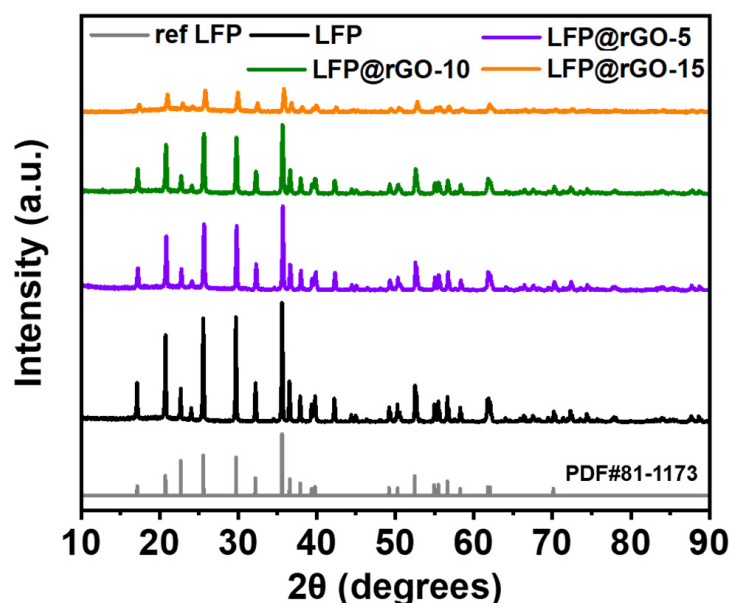

Figure 2. XRD patterns of LFP, LFP@rGO-5, LFP@rGO-10, and LFP@rGO-15 mAterials.

Raman analysis was performed to investigate the vibrational properties and confirm the presence of rGO in LFP composites, as shown in Figure 3a. The Raman spectra of LFP showed a prominent peak around 950 cm^{-1}, which corresponds to the symmetric stretching mode of the PO_4^{3-} group, a key feature for the olivine structure of LFP [57]. The Raman spectra of GO and plasma-treated rGO are shown in Figure S2. The mAin peaks of the D- and G-band were detected in the same region, but the ratio of the peaks was changed, confirming the successful rGO synthesis via the plasma-assisted photothermal reduction [58,59]. Additional peaks related to the carbon mAterial were observed for the LFP/rGO composites. Theoretically, the peaks appeared at 1350 and 1580 cm^{-1}, corresponding to the D- and G-bands. The D-band is associated with defects in the sp^2 carbon structure, while the G-band confirms the graphitic nature of rGO. The I_D/I_G ratio decreased from 0.90 in LFP@rGO-5 to 0.87 in LFP@rGO-15, indicating increased disorder and defects with higher rGO content. These results show that adding rGO improved the electrical conductivity and electrochemical performance of the composites.
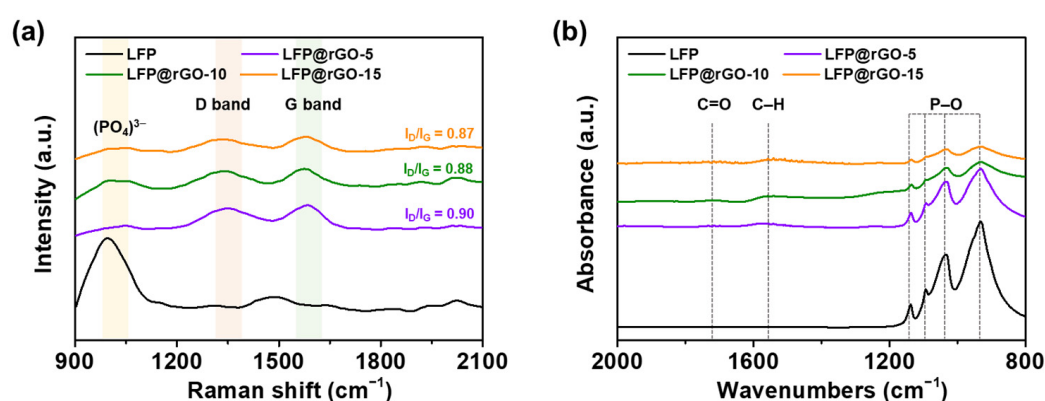

Figure 3. (**a**) Raman and (**b**) FT-IR spectra of LFP, LFP@rGO-5, LFP@rGO-10, and LFP@rGO-15.

Further, the functional group of the sample was analyzed by FT-IR, as shown in Figure 3b. LFP exhibited strong absorption bands around 1040 and 980 cm^{-1}, characteristic of the P–O stretching vibrations in the PO_4^{3-} group [60]. Bare GO and plasma-treated rGO showed peaks between 1800 and 800 cm^{-1}, as shown in Figure S3 [61]. The reduction of GO to rGO was confirmed by the absence of the OH peak at 3200 cm^{-1} [62]. The FT-IR spectra of the LFP@rGO composites showed additional bands around 2920 and 2850 cm^{-1}, which is associated with C–H stretching vibrations from residual organic groups in rGO and a peak around 1620 cm^{-1} corresponding to C=C stretching vibrations [63,64]. These findings confirmed the presence of rGO, whereas the characteristic P–O stretching bands of LFP remained visible, indicating that the LFP structure was mAintained. The increase in the intensity of the C–H and C=C bands with increasing rGO content, particularly in LFP@rGO-10 and LFP@rGO-15, aligns with the Raman spectra. Raman and FT-IR analyses confirmed the successful incorporation of rGO into the LFP mAtrix without significantly disrupting its structure, a key factor in preserving the electrochemical performance of the sample and improving its conductivity for energy storage applications.

3.2. Electrochemical Analysis of LFP@rGO Cathodes

The CV curves of LFP-, LFP@rGO-5-, LFP@rGO-10-, and LFP@rGO-15-based electrodes were systematically analyzed at scan rates of 0.1–2.0 mV s^{-1} to confirm rGO incorporation on the electrochemical performance, revealing distinct electrochemical behaviors, particularly in the potential range of 2.50–4.50 V (Figure 4a–d). All electrodes exhibited characteristic redox peaks corresponding to the reversible conversion between LiFePO$_4$ and FePO$_4$, which is a key process governed by the Fe^{2+}/Fe^{3+} redox couple [65]. Notably, the LFP electrode exhibited redox peaks at 3.80 V and 3.10 V at a scan rate of 0.1 mV s^{-1}, with a significant potential difference of 0.70 V, indicating relatively low charge transfer

kinetics [66]. In contrast, the LFP@rGO-10 electrode showed significant improvement, with redox peaks at 3.55 and 3.32 V, which results in a smaller potential difference of 0.23 V. This reduction in peak separation suggests enhanced electrochemical reversibility, which is attributed to optimal rGO coverage, facilitating better electron transport and mitigating polarization effects. Furthermore, the peak currents for LFP@rGO-10 were notably higher, with a larger integrated area under the CV curve, indicating the enhanced electrochemical capacity of the electrode. The anodic peak current increased from 1.32 to 2.02 mA, while the cathodic peak current changed from −1.01 to −1.66 mA. This implies that the optimal rGO coating not only improved the kinetic properties but also increased the overall capacity of the LFP@rGO composite mAterial. Electrodes with lower (LFP@rGO-5) and higher (LFP@rGO-15) rGO contents showed some improvement over the LFP; however, it did not mAtch the performance of the LFP@rGO-10 electrode, suggesting that the rGO content needs to be finely tuned to achieve the good electrochemical performance. In detail, LFP@rGO-5 exhibited redox peaks at 3.27 and 3.60 V with a peak current difference of 2.16 mA, while LFP@rGO-15 showed peaks at 3.31 and 3.55 V with a peak current difference of 2.91 mA. The optimization of rGO is important because excessive rGO can lead to agglomeration, reducing the effectiveness of the coating, whereas insufficient rGO cannot fully exploit its conductive properties. Detailed quantitative data on redox potentials, peak currents across different electrodes, and scan rates are summarized in Table S1, further supporting these findings.
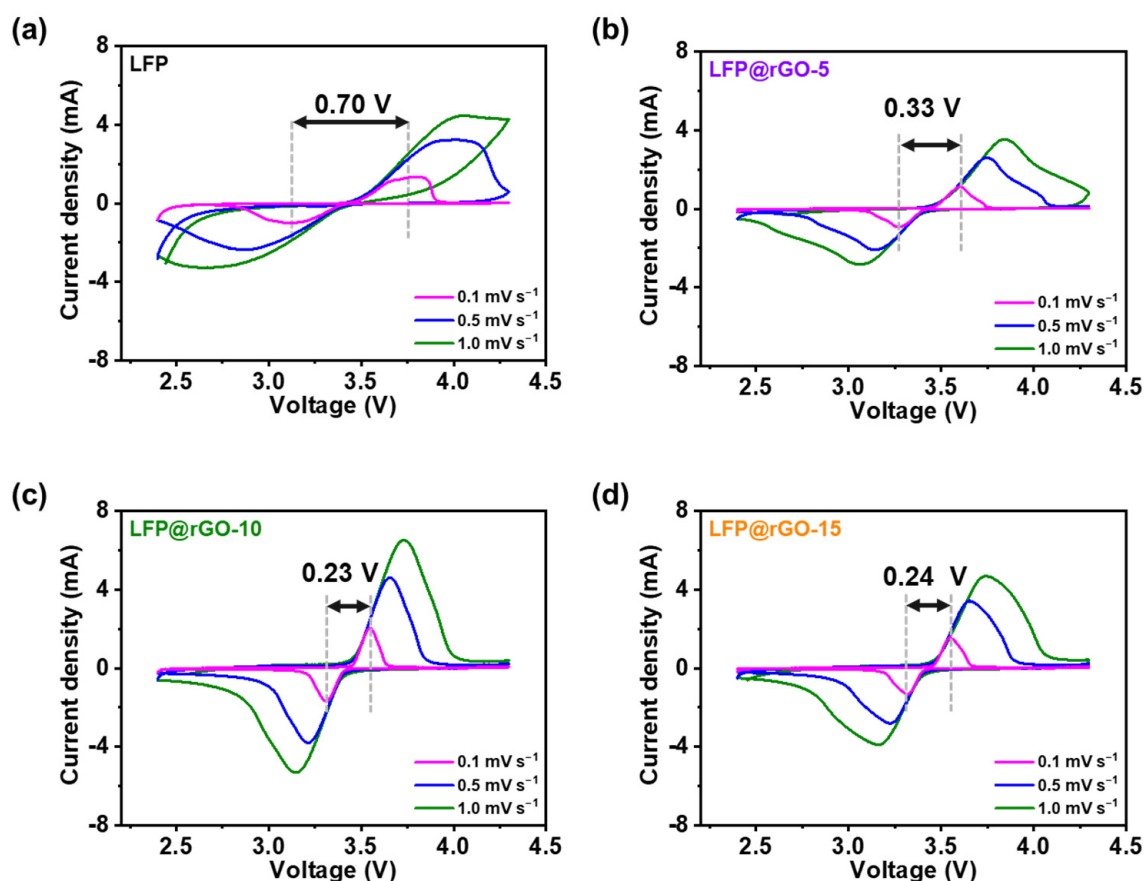

Figure 4. CV curves of (**a**) LFP-, (**b**) LFP@rGO-5-, (**c**) LFP@rGO-10-, and (**d**) LFP@rGO-15-based electrodes.

Charge and discharge curves were examined across different C-rates ranging from 0.1 to 2.0 C within a potential window of 2.50–4.30 V (Figure 5a–d) to further investigate the electrochemical performance of the LFP- and LFP@rGO-based electrodes. LFP has stable electrochemical performance and safety, mAking it a popular choice for LIBs [67]. However, their relatively low electrical conductivities limit their rate capabilities. To address

these limitations, rGO was incorporated to enhance conductivity and overall electrode performance. The recorded curves showed distinct plateau regions at ca. 3.44 V during both charging and discharging, consistent with the potential peaks observed in the CV curves and indicating the LFP redox reaction, which involves the reversible lithium ions (de)intercalation within the LFP structure. The expansion of these plateau regions with increasing C-rate indicates higher polarization of the electrodes, a common characteristic at higher current densities. This occurs due to resistance within the electrode mAterial and electrolyte, which becomes more noticeable at higher current rates. Among the tested electrodes, the LFP@rGO-10-based electrode delivered the highest discharge capacities of 164.9, 162.2, 154.8, 142.7, and 129.8 mAh g^{-1} at C-rates of 0.1, 0.2, 0.5, 1.0, and 2.0 C, respectively. The obtained capacities were 1.13-, 1.14-, 1.15-, 1.47-, and 1.89-fold higher than those of the pure LFP-based electrode, demonstrating a significant enhancement in performance attributable to the optimized rGO content. Further, the LFP@rGO-10 electrode exhibited excellent coulombic efficiencies of 99.9, 99.8, 99.5, 99.4, and 95.5% at the corresponding C-rates, highlighted the superior reversibility and electrochemical stability achieved with the incorporation of 10.0 wt% rGO. This enhancement is attributed to the high electrical conductivity of rGO, which facilitates efficient ion transfer pathways and reduces internal resistance. Figure 5e shows the rate capabilities of the LFP- and LFP@rGO-based electrodes over five cycles at different C-rates. Remarkably, the LFP@rGO-10-based electrode retained 95.0% of its capacity at 0.1 C even after 25 cycles at different C-rates, further confirming its outstanding reversibility and durability. In addition, the charge/discharge capacity and rate capability of the LFP@C-10-based electrode were measured to compare the performance improvement of coating commercially available carbon mAterial on LFP (Figure S4). The LFP@C-10-based electrode exhibited a stable behavior, with discharge capacities of 153.0, 151.0, 143.3, 118.4, and 91.4 mAh g^{-1} at C-rates of 0.1, 0.2, 0.5, 1.0, and 2.0 C, respectively. Although the obtained capacities were higher than those of the LFP-based electrode, the enhancement was less compared to the LFP@rGO-10-based electrode. This mAy be attributed to the superior Li-ion diffusion properties of rGO compared to commercially available carbon mAterial due to rGO's intrinsic characteristics, such as high surface area and mesoporous structure. The detailed rate performance data and coulombic efficiencies for LFP-, LFP@rGO-5-, LFP@rGO-10-, LFP@rGO-15-, and LFP@C-10-based electrodes are summarized in Table S2.

To gain deeper insight into the resistive and the capacitive properties of the electrodes, EIS analysis was conducted. The resulting Nyquist plots, where each plot presents a semicircle followed by a linear segment indicating a different electrochemical reaction, are displayed in Figures 5f and S5. The equivalent circuit model, shown as an inset in the EIS, includes components such as ohmic resistance (R_S), charge transfer resistance (R_{CT}), double-layer capacitance (CPE), and Warburg impedance (Z_W) [68]. R_S, shown at the x-axis intercept in the high-frequency region, represents the total resistance of the electrode, electrolyte, and separator [69], influencing battery efficiency. The semicircle in the medium-frequency range corresponds to R_{CT}, associated with the electrode-electrolyte interface [70]; a smaller semicircle suggests reduced charge-transfer resistance, improving electrochemical performance. The inclined line in the low-frequency region reflects Z_W, linked to lithium-ion diffusion in LFP, which is essential for mAintaining high capacity and rate performance [71]. The LFP@rGO-10-based electrode exhibited the smallest semicircle diameter, indicating the lowest R_{CT} and most efficient ion transfer among the electrodes. The measured R_{CT} for the LFP-, LFP@rGO-5-, LFP@rGO-10-, LFP@rGO-15-, and LFP@C-10-based electrodes were 306.0, 269.6, 226.4, 262.3, and 253.1 Ω, respectively. These findings confirm that the optimal incorporation of rGO significantly enhances the electrochemical performance of cathodes by reducing charge transfer resistance and creating a conductive network that facilitates faster electron and ion transport.
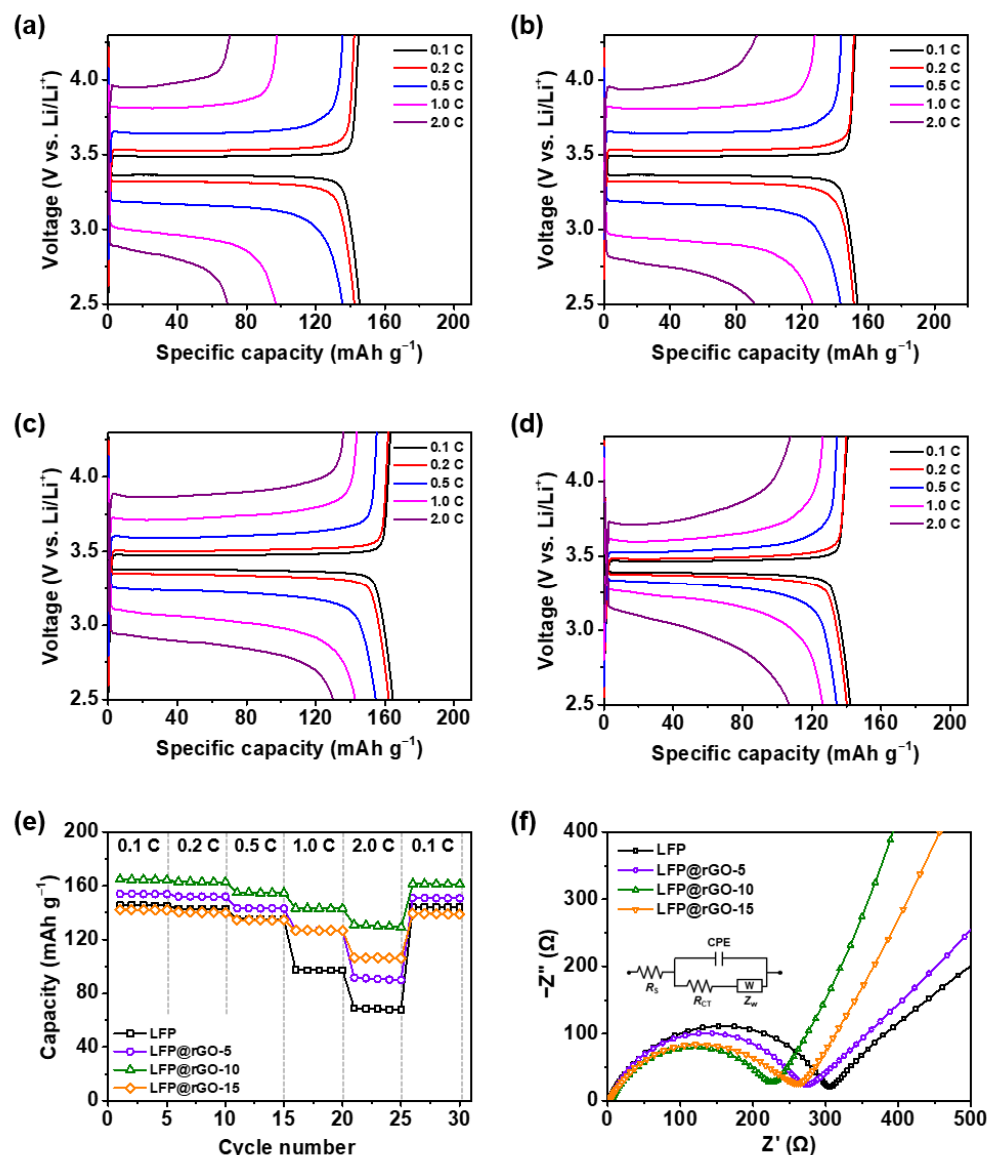
Figure 5. Charge/discharge curves of (**a**) LFP-, (**b**) LFP@rGO-5-, (**c**) LFP@rGO-10-, and (**d**) LFP@rGO-15-based electrodes in the half-cell at various current rates (C-rates) from 0.1 to 2.0 C. (**e**) Rate capability test and (**f**) EIS Nyquist plots of the electrodes.

3.3. Practical LIB Application of the LFP@rGO//Graphite Full-Cell

A LIB full-cell was assembled using LFP@rGO-10 as the cathode and graphite as the anode (LFP@rGO-10//graphite cell) to evaluate the potential of LFP@rGO-10 as an energy-storage system. LFP is known for its excellent thermal stability and safety; however, its low electrical conductivity limits its performance. To overcome this limitation, rGO was used to enhance the conductivity and overall performance of the electrodes. A comparative LIB cell (LFP//graphite) was assembled using LFP as the cathode with all other assembly conditions identical to those of the LFP@rGO-10//graphite cell to confirm the enhancement provided by rGO. The charge/discharge curves for both LFP//graphite and LFP@rGO-10//graphite cells were evaluated across a range of C-rates from 0.1 to 2.0 C, as shown in Figure 6a,b. Figure 6c shows the specific capacity values at different C-rates, confirming that the LFP@rGO-10//graphite cell achieved higher specific capacity than the LFP//graphite cell across various C-rates. The LFP//graphite cell exhibited specific capacities of 120.0, 113.0, 105.0, 85.6, and 58.2 mAh g^{-1} at 0.1, 0.2, 0.5, 1.0, and 2.0 C, respectively, while the LFP@rGO-10//graphite cell delivered specific capacities of

147.5, 143.6, 135.7, 119.8, and 94.3 mAh g^{-1} under the same conditions. This remarkable enhancement in the performance of the LFP@rGO-10//graphite cell is attributed to the effective rGO coating, which enhances the intrinsic electrical conductivity of LFP. The conductive rGO layer facilitated better electron transport, reduced overall resistance, and improved cell charge/discharge efficiency. In addition, the LFP@rGO-10//graphite cell exhibited high coulombic efficiencies in all C-rates, as shown in Figure 6d, confirming the beneficial role of rGO in enhancing electrochemical performance. Such a high coulombic efficiency for the LFP@rGO-10//graphite cell was ascribed to the rGO with a high surface owing to its large surface-to-volume ratio, which provides more active sites for lithium-ion adsorption and intercalation, enabling the achievement of a high charge/discharge rate and structural integrity, and the protective barrier layer formed by the rGO reduces undesirable side reactions, leading to a high coulombic efficiency [72–74]. The superior performance and efficiency observed in the LFP@rGO-10//graphite cell emphasize the potential of rGO-modified LFP as a promising cathode mAterial for high-performance LIBs, offering both enhanced capacity and stability. These findings highlight the importance of optimizing the electrode mAterials to achieve enhanced performance for LIB, particularly in terms of energy density, cycling stability, and rate capability.
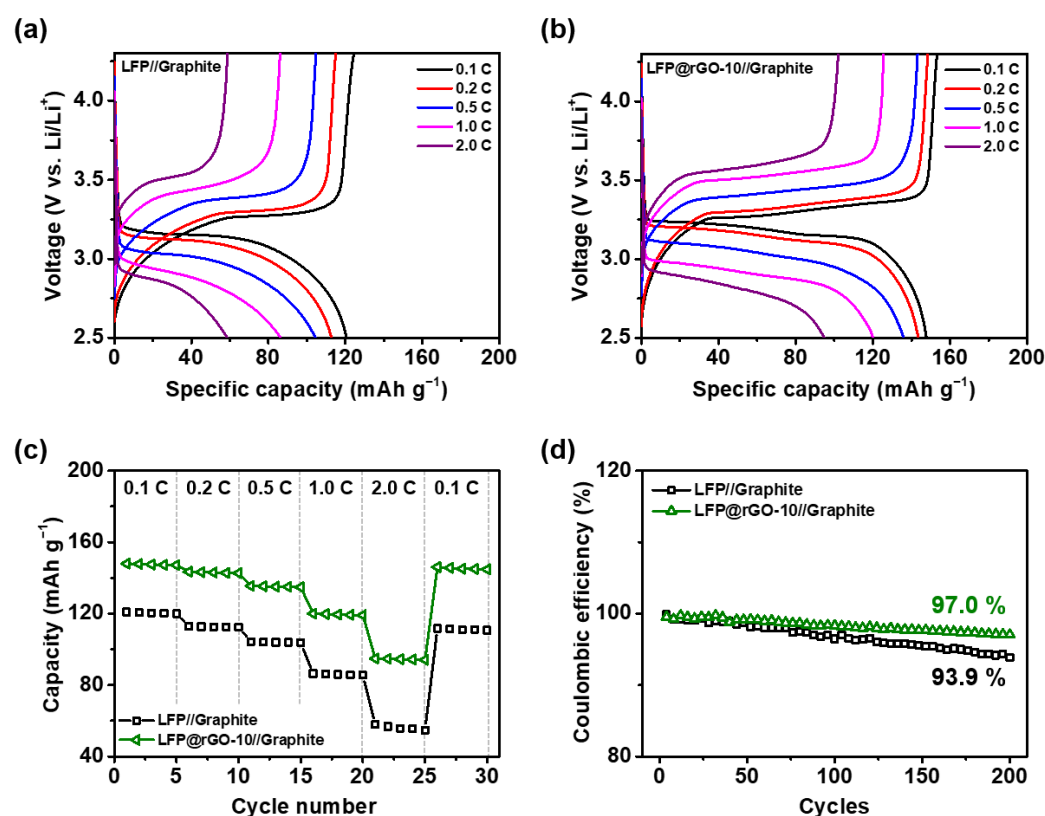

Figure 6. Charge/discharge curves of (**a**) LFP//graphite and (**b**) LFP@rGO-10//graphite LIB full-cells at various C-rates. (**c**) Specific capacities and (**d**) coulombic efficiencies of LIB cells calculated from charge/discharge curves.

The lithium-ion transfer abilities of the LFP//graphite and LFP@rGO-10//graphite full-cells were further investigated using EIS analysis, and the corresponding Nyquist plots after the initial cycle are shown with an equivalent circuit (Figure 7a). The R_{CT} values, which mostly affect the cell impedance, for LFP//graphite and LFP@rGO-10//graphite cells were 113.3 and 101.7 Ω, respectively. It can be determined that the lithium-ion transfer

characteristics of LFP-based electrodes were improved by adding the optimal amount of rGO. The Li-ion diffusion coefficients (D_{Li+}) were calculated using Equations (1) and (2):

$$Z' = R_s + R_{CT} + \sigma\omega^{-1/2} \tag{1}$$

$$D_{Li+} = \frac{R^2 T^2}{2A^2 n^4 F^4 C_{Li+}{}^2 \sigma^2}, \tag{2}$$

where Z', $\omega^{-1/2}$, R, T, A, n, F, C_{Li+}, and σ represent the real part of the impedance, reciprocal square root of the frequency in the low-frequency region, gas constant (8.314 J mol^{-1} K^{-1}), absolute temperature, surface area of the electrode (1.54 cm^2), number of electrons transferred during oxidization, Faraday's constant ($96,485.33$ C mol^{-1}), concentration of lithium ion (0.0288 mol cm^3), and Warburg factor, respectively [75].
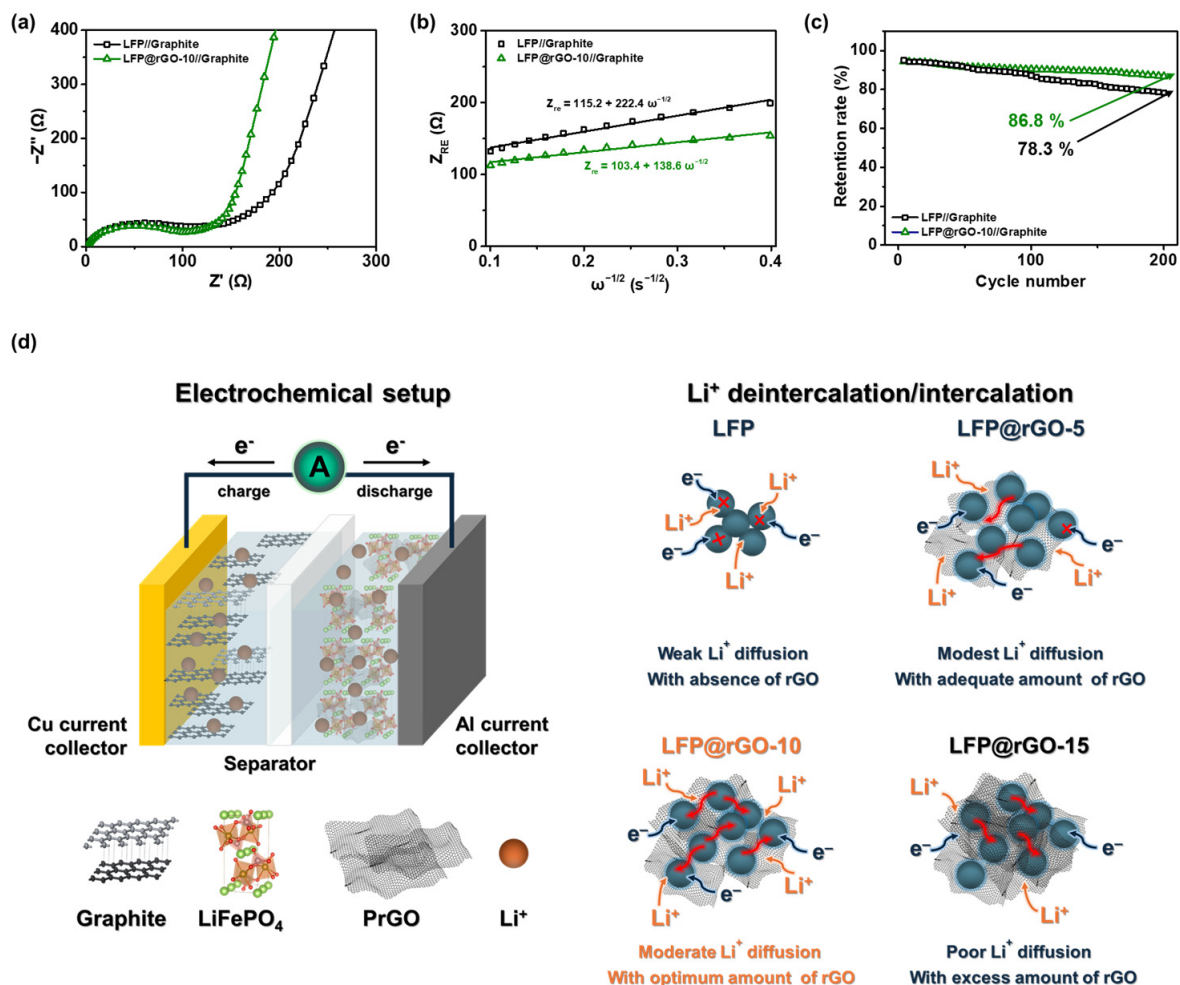

Figure 7. (**a**) EIS Nyquist plot and (**b**) the fitting curves of Z_{RE} and $\omega^{-1/2}$. (**c**) Cyclability test results of LFP//graphite and LFP@rGO-10//graphite LIB cells after 200 cycles at 0.2 C. (**d**) Tentative mechanism of the improved electrochemical performance of LFP@rGO-10.

Figure 7b shows the relationship between Z_{Re} and $\omega^{-1/2}$ for the LFP//graphite and LFP@rGO-10//graphite cells. The slope of the fitting curves, which represents σ, was calculated to be 222.4 and 138.6 Ω s$^{-1/2}$. The D_{Li+} values of the LFP//graphite and LFP@rGO-10//graphite cells were calculated to be 3.64×10^{-16} and 9.37×10^{-16} cm^2 s^{-1}, respectively, indicating that the LFP@rGO-10//graphite cell exhibited higher lithium-ion diffusion coefficient. The calculation results confirmed that the incorporation of an optimal amount of rGO effectively enhanced the lithium-ion diffusion rate in LFP. The cycling performances of the LFP//graphite and LFP@rGO-10//graphite cells were evaluated after

charging and discharging at 0.2 C for 200 cycles (Figure 7c). After cycling, the LFP@rGO-10//graphite cell retained 86.8% of its initial capacity, which was significantly higher than the 78.3% retention measured in the LFP//graphite cell. This enhanced performance can be attributed to the improved ion diffusion rate facilitated by the rGO, which enhanced the ion transport capability. Consequently, the electrochemical analysis results confirm that incorporating an optimal amount of rGO into the LFP cathode substantially improves the electrochemical performance of LIBs, offering both enhanced capacity retention and stability over extended cycling.

To observe the evolution of R_{CT} over time, EIS analysis was conducted on LFP//graphite and LFP@rGO-10//graphite full-cells after 100 charge/discharge cycles at 0.2 C, and the results are shown in the Nyquist plots (Figure S6a). It was clear that another semicircle was observed for both LFP//graphite and LFP@rGO-10//graphite cells, attributed to the formation of a solid electrolyte interface (SEI) layer on the surface of graphite anode during the cycling processes. The corresponding Z_{RE} and $\omega^{-1/2}$ fitting curves of both cells are shown in Figure S6b. The y-intercept values expressing the internal resistance for LFP//graphite and LFP@rGO-10//graphite cells were measured as 160.3 and 126.5 Ω, respectively. The corresponding R_{CT} values were then obtained as 157.7 and 123.6 Ω. Compared to those after the initial cycle, the R_{CT} values of LFP//graphite and LFP@rGO-10//graphite cells increased by 47.0 and 24.8 Ω after 100 cycles. This was mAinly due to the formation of the SEI layer, lowering electrochemical performance. The Li$^+$ diffusion rate of both cells after 100 cycles was evaluated using Equation (2), showing $D_{\mathrm{Li+}}$ values of 2.75 $\times$ 10^{-16} and 5.14 $\times$ 10^{-16} cm^2 s^{-1}. Although $D_{\mathrm{Li+}}$ of both cells after 100 cycles decreased compared to that after the initial cycle due to the degradation of electrolyte during cycling processes, the LFP@rGO-10//graphite cell showed a higher Li$^+$ diffusion rate. Accordingly, the EIS analysis of LFP//graphite and LFP@rGO-10//graphite cells over cycling processes confirmed both the change in resistance and Li$^+$ diffusion rate.

The fundamental working mechanism of the LIB is discussed to explain the difference in electrochemical performance in detail. The decay in the electrochemical performance of the LFP//graphite full-cell is described as follows. During the charging mechanism, lithium ions (Li$^+$) are extracted from the LFP cathode, forming FePO$_4$, and migrate toward the graphite anode through the electrolyte. During discharge, Li$^+$ ions are released from graphite and re-intercalate into the LFP cathode. Over prolonged charge/discharge cycling, the LFP structure degrades, reducing the number of active Li$^+$ intercalation sites. This degradation, along with electrolyte decomposition and byproduct formation, blocks the Li$^+$ transport channels and increases the internal resistance, leading to a gradual decrease in the LIB full-cell capacity and overall performance. The substantially improved electrochemical performance of the LFP@rGO-10 cathode is further explained in the following section. Figure 7d shows the underlying charge carrier mechanism of the LIB with LFP@rGO-10 as the cathode and graphite as the anode.

In a lithium-ion battery (LIB) using LFP@rGO as the cathode and graphite as the anode, the charge-carrier mechanism involves several electrochemical steps. During charging, Li$^+$ moves from the electrolyte to the graphite anode, where they intercalate themselves between the graphene layers. This process is aided by electrons from the external circuit, which neutralize the Li$^+$ ions as they reach the anode. At the LFP@rGO cathode, the applied voltage extracts Li$^+$ ions from the LFP structure (Equation (3)). The rGO component improves the conductivity of LFP, allowing Li$^+$ ions to move more easily and reducing resistance. As electrons flow into the cathode, they drive an oxidation reaction, releasing Li$^+$ ions into the electrolyte. The olivine structure of LFP undergoes a redox reaction, where Li$^+$ is extracted, and Fe^{2+} is oxidized to Fe^{3+}, resulting in the formation of FePO$_4$. These released Li$^+$ ions travel through the electrolyte to the graphite anode, where they intercalate between the graphite layers. Electrons from an external power source reduce the lithium ions, forming LiC$_6$ (Equation (4)). During discharge, this process is reversed. Li$^+$ ions leave the graphite anode and move back into the electrolyte while electrons flow through the external circuit to the cathode. The Li$^+$ ions are then reinserted into the LFP

structure, with electrons aiding their reduction. This intercalation process relies on solid-state diffusion in LFP and the weak van der Waals forces in graphite, which together ensure efficient charging and discharging cycles. The rGO addition enhances the electronic conductivity of the cathode, leading to improved battery performance, particularly in terms of charge/discharge speed and stability. Overall, the LFP@rGO cathode, with improved conductivity and structural stability from rGO, combined with the graphite anode's reliable intercalation properties, contributes to the high performance of the LIB. The intercalation and deintercalation processes, along with the efficient transport of electrons and ions enabled by rGO, are key factors in achieving high energy density, fast charge/discharge rates, and long-term cycling stability in these batteries.

Charging mechanism:

$$LiFePO_4 \rightarrow FePO_4 + Li^+ + e^- \tag{3}$$
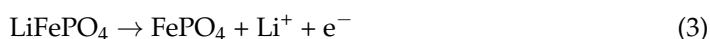
Lithium intercalation in anode mAterial:

$$C_6 + Li^+ + e^- \rightarrow LiC_6 \tag{4}$$

The relationship between energy and power densities, highlighting the trade-off between energy storage and delivery speed, is summarized in Table 2. In an LIB with an LFP@rGO cathode and graphite anode, significant improvements in both energy and power densities were observed compared to conventional $LiFePO_4$ systems. While $LiFePO_4$ is known for its thermal stability and long cycle life, its low electrical conductivity and moderate lithium-ion diffusion rates limit power density. The incorporation of rGO improves conductivity by creating a conductive network, reducing internal resistance, and enabling faster electron and ion transport. This boosts power density without compromising energy density. Graphite, used as the anode, supports high energy density due to its ability to intercalate Li^+ ions at low voltages. The synergy between the LFP@rGO cathode and graphite anode achieves a balance between high energy density and improved power capabilities, allowing the battery to sustain high energy output at fast discharge rates. This indicates that the battery can handle high-current demands efficiently, mAking it suitable for high-power and high-energy applications. Additionally, rGO enhances the mechanical stability of LFP particles, improving cycling stability and extending battery life for devices requiring consistent performance over mAny charge-discharge cycles. The combination of high energy density, power density, and durability mAkes LFP@rGO an excellent choice for modern energy storage systems.

Table 2. Comparison of capacity of LFP-rGO-10-based electrode with other LFP-based electrodes.

Electrode mAterial	Precursor	Capacity (mAh g^{-1})	Ref.
NSC@LFP	Methionine	103.0 at 2.0 C	[76]
3D-MCC-LFP$_{10}$	MXene and CNTs	85.9 at 5.0 C	[77]
LFP/EGO	Exfoliated graphene oxide	61.7 at 2.0 C	[78]
C/LCP-2	Cellulose	90 at 2.0 C	[79]
LFP/C-15	Glucose	124.9 at 2.0 C	[80]
LFP@rGO-10	rGO	94.3 at 2.0 C	This work

4. Conclusions

In this study, $LiFePO_4$@rGO was fabricated by freeze drying and plasma treatment. A porous structure induced by plasma treatment was formed in GO, resulting in the formation of ion transfer channels. The amount of rGO added to the LFP was adjusted from 5.0 to 15.0 wt% to achieve the highest electrochemical performance. With the optimum rGO content, the surface of the LFP was uniformly covered by the sheet, forming a continuous conductive network. In the half-cell test, the cathode composed of LFP@rGO-10 exhibited the highest discharge capacity of 142.7 mAh g^{-1} at 1.0 C-rates with a remarkable capacity of 95.0% even after 25 cycling tests, thereby confirming the outstanding reversibility and

durability of the electrode. A LIB full-cell was assembled using LFP@rGO-10 as the cathode and graphite as the anode. The LFP@rGO-10//graphite full-cell exhibited a higher specific capacity than the LFP//graphite full-cell at various C-rates with high coulombic efficiencies, resulting from efficient electron and ion transport facilitated by rGO, which is crucial for achieving high energy density, rate capability, and long-term cycling stability in LIB. The outstanding efficiency and performance of the LFP@rGO-10//graphite cell highlight the promising potential of rGO-modified LFP as a cathode mAterial for high-performance LIBs, providing both increased capacity and stability.

Supplementary Materials: The following supporting information can be downloaded at: https://www.mdpi.com/article/10.3390/batteries10100345/s1, Figure S1: Low- and high-magnification SEM micrographs of (a,b) graphene oxide (GO) and (c,d) reduced graphene oxide (rGO). Figure S2: Raman spectra of GO and rGO. Figure S3: FT-IR spectra of GO and rGO. Table S1: Redox potentials of LFP-, LFP@rGO-5-, LFP@rGO-10-, and LFP@rGO-15-based electrodes at various scan rates. Figure S4: (a) Charge/discharge curves and (b) rate capability test results of the LFP@C-10-based electrode. Table S2: Charge/discharge capacities and coulombic efficiencies of LFP-, LFP@rGO-5-, LFP@rGO-10-, LFP@rGO-15-, and LFP@C-10-based electrodes at various C-rates. Figure S5: EIS Nyquist plot of the LFP@C-10-based electrode. Figure S6: (a) EIS Nyquist plot and (b) the fitting curves of Z_{RE} and $\omega^{-1/2}$ of the LFP//graphite and LFP@rGO-10//graphite full-cells after 100 cycles at 0.2 C.

Author Contributions: S.J. and C.-G.K.: Conceptualization, Formal Analysis, Investigation, Validation, Data Curation, Writing—Original Draft, Writing—Review and Editing; J.K. and H.-Y.K.: Investigation, Validation, Data Curation, Writing—Original Draft; Y.-R.C.: Investigation, Validation, Writing—Review and Editing; Y.-H.R.: Visualization, Validation, Data Curation; Z.O.: Conceptualization, Investigation, Visualization, Methodology, Data Curation, Writing—Original Draft, Writing—Review and Editing; C.-M.Y.: Conceptualization, Formal Analysis, Investigation, Validation, Visualization, Methodology, Data Curation, Writing—Original Draft, Writing—Review and Editing, Supervision, Project Administration, Funding Acquisition. All authors have read and agreed to the published version of the mAnuscript.

Data Availability Statement: Data are contained within the article.

Conflicts of Interest: The authors declare no conflicts of interest.

References

1. Larcher, D.; Tarascon, J.M. Towards greener and more sustainable batteries for electrical energy storage. *Nat. Chem.* **2015**, *7*, 19–29. [CrossRef] [PubMed]
2. Yang, Y.; Okonkwo, E.G.; Huang, G.; Xu, S.; Sun, W.; He, Y. On the sustainability of lithium ion battery industry—A review and perspective. *Energy Storage mAter.* **2021**, *36*, 186–212. [CrossRef]
3. Liu, C.; Li, F.; mA, L.P.; Cheng, H.M. Advanced mAterials for energy storage. *Adv. mAter.* **2010**, *22*, E28–E62. [CrossRef]
4. Xie, C.; Chang, J.; Shang, J.; Wang, L.; Gao, Y.; Huang, Q.; Zheng, Z. Hybrid lithium-ion/metal electrodes enable long cycle stability and high energy density of flexible batteries. *Adv. Funct. mAter.* **2022**, *32*, 2203242. [CrossRef]
5. Khan, F.N.U.; Rasul, M.G.; Sayem, A.S.M.; mAndal, N.K. Design and optimization of lithium-ion battery as an efficient energy storage device for electric vehicles: A comprehensive review. *J. Energy Storage* **2023**, *71*, 108033. [CrossRef]
6. Chen, D.; Lou, Z.; Jiang, K.; Shen, G. Device configurations and future prospects of flexible/stretchable lithium-ion batteries. *Adv. Funct. Mater.* **2018**, *28*, 1805596. [CrossRef]
7. Kim, T.H.; Park, J.S.; Hang, S.K.; Choi, S.; Ryu, J.H.; Song, H.K. The current move of lithium ion batteries towards the next phase. *Adv. Energy mAter.* **2012**, *2*, 860–872. [CrossRef]
8. Liu, Z.; Jiang, Y.; Hu, Q.; Guo, S.; Yu, L.; Li, Q.; Liu, Q.; Hu, X. Safer lithium-ion batteries from the separator aspect: Development and future perspectives. *Energy Environ. mAter.* **2021**, *4*, 336–362. [CrossRef]
9. Li, Y.; Tan, Z. Effects of a separator on the electrochemical and thermal performances of lithium-ion batteries: A numerical study. *Energy Fuels* **2020**, *34*, 14915–14923. [CrossRef]

10. Guo, Z.; Liu, Z.; Chen, W.; Sun, X.; Zhang, X.; Wang, K.; mA, Y. Battery-Type Lithium-Ion Hybrid Capacitors: Current Status and Future Perspectives. *Batteries* **2023**, *9*, 74. [CrossRef]

11. Goriparti, S.; Miele, E.; De Angelis, F.; Di Fabrizio, E.; Zaccaria, R.P.; Capiglia, C. Review on recent progress of nanostructured anode mAterials for Li-ion batteries. *J. Power Sources* **2014**, *257*, 421–443. [CrossRef]

12. Lee, S.; Hong, J.; Kang, K. Redox-active organic compounds for future sustainable energy storage system. *Adv. Energy mAter.* **2020**, *10*, 2001445. [CrossRef]

13. Di Lecce, D.; Verrelli, R.; Hassoun, J. Lithium-ion batteries for sustainable energy storage: Recent advances towards new cell configurations. *Green Chem.* **2017**, *19*, 3442–3467. [CrossRef]

14. Kotal, M.; Jakhar, S.; Roy, S.; Sharma, H.K. Cathode mAterials for rechargeable lithium batteries: Recent progress and future prospects. *J. Energy Storage* **2022**, *47*, 103534. [CrossRef]

15. Kim, J.S.; Lim, S.; Ingole, R.S.; Munakata, H.; Kim, S.S.; Kanamura, K. Improving the high-rate performance of LCO cathode by metal oxide coating: Evaluation using single particle measurement. *J. Electroanal. Chem.* **2023**, *933*, 117190. [CrossRef]

16. Cai, W.F.; Chen, K.C. Influence of the Calendar Aging on the Cycle Aging of $LiNiMnCoO_2$ lithium-Ion Batteries. *J. Electrochem. Soc.* **2021**, *168*, 120525. [CrossRef]

17. Joos, J.; Buchele, A.; Schmidt, A.; Weber, A.; Ivers-Tiffée, E. Virtual Electrode Design for Lithium-Ion Battery Cathodes. *Energy Technol.* **2021**, *9*, 2000891. [CrossRef]

18. Wang, L.; Chen, B.; mA, J.; Cui, G.; Chen, L. Reviving lithium cobalt oxide-based lithium secondary batteries-toward a higher energy density. *Chem. Soc. Rev.* **2018**, *47*, 6505–6602. [CrossRef]

19. Li, W.; Lee, S.; mAnthiram, A. High-nickel NMA: A cobalt-free alternative to NMC and NCA cathodes for lithium-ion batteries. *Adv. mAter.* **2020**, *32*, 2002718. [CrossRef]

20. Ding, Y.; Cano, Z.P.; Yu, A.; Lu, J.; Chen, Z. Automotive Li-ion batteries: Current status and future perspectives. *Electrochem. Energy Rev.* **2019**, *2*, 1–28. [CrossRef]

21. Zhou, T.; Sun, J.; Li, J.; Wei, S.; Chen, J.; Dang, S.; Tang, N.; Zhu, Y.; Lian, Y.; Gao, J.; et al. Toxicity, Emissions and Structural Damage from Lithium-Ion Battery Thermal Runaway. *Batteries* **2023**, *9*, 308. [CrossRef]

22. Yi, M.; Li, W.; mAnthiram, A. Delineating the roles of Mn, Al, and Co by comparing three layered oxide cathodes with the same nickel content of 70% for lithium-ion batteries. *Chem. mAter.* **2022**, *34*, 629–642. [CrossRef]

23. Ohneseit, S.; Finster, P.; Floras, C.; Lubenau, N.; Uhlmann, N.; Seifert, H.J.; Ziebert, C. Thermal and mechanical safety assessment of type 21700 lithium-ion batteries with NMC, NCA and LFP cathodes–Investigation of cell abuse by means of accelerating rate calorimetry (ARC). *Batteries* **2023**, *9*, 237. [CrossRef]

24. Mauger, A.; Julien, C.M. Olivine positive electrodes for Li-ion batteries: Status and perspectives. *Batteries* **2018**, *4*, 39. [CrossRef]

25. Wang, Y.; Li, R.; Feng, B.; Long, T.; Wang, K.; Yu, Q.; Wang, Z.; Ding, Y.L. Enabling fast charging and all-climate Mn-containing olivine cathode via constructing hierarchically porous bulk architecture. *J. Power Sources* **2024**, *614*, 234996. [CrossRef]

26. Suttison, S.; Pengpat, K.; Intatha, U.; Fan, J.; Zhang, W.; Eitssayeam, S. Preparation of LFP-based cathode mAterials for lithium-ion battery applications. *Mater. Today Proc.* **2022**, *65*, 2347–2350. [CrossRef]

27. Andrews, J.L.; Brady, M.J.; McClure, E.T.; Melot, B.C. Impact of structural deformations on the performance of Li-ion insertion hosts. *Chem. mAter.* **2022**, *34*, 4809–4820. [CrossRef]

28. Rkhis, M.; Laasri, S.; Touhtouh, S.; Hlil, E.K.; Hajjaji, A. Tailoring the electrochemical performance of olivine phosphate cathode mAterials for Li-Ion batteries by strain engineering: Computational experiments. *ACS Appl. Energy mAter.* **2023**, *6*, 7074–7082. [CrossRef]

29. Chen, S.P.; Lv, D.; Chen, J.; Zhang, Y.H.; Shi, F.N. Review on defects and modification methods of $LiFePO_4$ cathode mAterial for lithium-ion batteries. *Energy Fuels* **2022**, *36*, 1232–1251. [CrossRef]

30. Varzi, A.; Bresser, D.; von Zamory, J.; Müller, F.; Passerini, S. $ZnFe_2O_4$-C/$LiFePO_4$-CNT: A novel high-power lithium-ion battery with excellent cycling performance. *Adv. Energy mAter.* **2014**, *4*, 1400054. [CrossRef]

31. Huang, C.Y.; Kuo, T.R.; Yougbaré, S.; Lin, L.Y. Design of $LiFePO_4$ and porous carbon composites with excellent High-Rate charging performance for Lithium-Ion secondary battery. *J. Colloid Interface Sci.* **2022**, *607*, 1457–1465. [CrossRef]

32. Wang, J.; Sun, X. Understanding and recent development of carbon coating on $LiFePO_4$ cathode mAterials for lithium-ion batteries. *Energy Environ. Sci.* **2012**, *5*, 5163–5185. [CrossRef]

33. Peng, J.M.; Chen, Z.Q.; Li, Y.; Hu, S.-J.; Pan, Q.-C.; Zheng, F.-H.; Wang, H.-Q.; Li, Q.-Y. Conducting network interface modulated rate performance in $LiFePO_4$/C cathode mAterials. *Rare Met.* **2022**, *41*, 951–959. [CrossRef]

34. Napolskiy, F.; Avdeev, M.; Yerdauletov, M.; Ivankov, O.; Bocharova, S.; Ryzhenkova, S.; Kaparova, B.; Mironovich, K.; Burlyaev, D.; Krivchenko, V. On the Use of Carbon Nanotubes in Prototyping the High Energy Density Li-ion Batteries. *Energy Technol.* **2020**, *8*, 2000146. [CrossRef]

35. Jiang, W.; Wu, M.; Liu, F.; Yang, J.; Feng, T. Variation of carbon coatings on the electrochemical performance of $LiFePO_4$ cathodes for lithium ionic batteries. *RSC Adv.* **2017**, *7*, 44296–44302. [CrossRef]

36. Ramasubramanian, B.; Sundarrajan, S.; Chellappan, V.; Reddy, M.V.; Ramakrishna, S.; Zaghib, K. Recent Development in Carbon-$LiFePO_4$ Cathodes for Lithium-Ion Batteries: A Mini Review. *Batteries* **2022**, *8*, 133. [CrossRef]

37. Kim, J.; Kim, M.; Cho, S.; Yoon, C.-M.; Lee, C.; Ryu, J.; Jang, J. Multidimensional polyaniline/reduced graphene oxide/silica nanocomposite for efficient supercapacitor electrodes. *ChemNanoMat* **2016**, *2*, 236–241. [CrossRef]

38. Noh, J.; Jekal, S.; Yoon, C.-M. Polyaniline-Coated Mesoporous Carbon Nanosheets with Fast Capacitive Energy Storage in Symmetric Supercapacitors. *Adv. Sci.* **2023**, *10*, 2301923. [CrossRef]

39. Wasalathilake, K.C.; Li, H.; Xu, L.; Yan, C. Recent advances in graphene based mAterials as anode mAterials in sodium-ion batteries. *J. Energy Chem.* **2020**, *42*, 91–107. [CrossRef]

40. Voiry, D.; Yang, J.; Kupferberg, J.; Fullon, R.; Lee, C.; Jeong, H.Y.; Shin, H.S.; Chhowalla, M. High-quality graphene via microwave reduction of solution-exfoliated graphene oxide. *Science* **2016**, *353*, 1413–1416. [CrossRef]

41. Kumar, H.; Sharma, R.; Yadav, A.; Kumari, R. Recent advancement mAde in the field of reduced graphene oxide-based nanocomposites used in the energy storage devices: A review. *J. Energy Storage* **2021**, *33*, 102032. [CrossRef]

42. Lee, J.H.; Park, N.; Kim, B.G.; Jung, D.S.; Im, K.; Hur, J.; Choi, J.W. Restacking-inhibited 3D reduced graphene oxide for high performance supercapacitor electrodes. *ACS Nano* **2013**, *7*, 9366–9374. [CrossRef]

43. Cui, C.; Qian, W.; Yu, Y.; Kong, C.; Yu, B.; Xiang, L.; Wei, F. Highly electroconductive mesoporous graphene nanofibers and their capacitance performance at 4 V. *J. Am. Chem. Soc.* **2014**, *136*, 2256–2259. [CrossRef]

44. Lee, G.; Lee, C.; Yoon, C.-M.; Kim, M.; Jang, J. High-performance three-dimensional mesoporous graphene electrode for supercapacitors using lyophilization and plasma reduction. *ACS Appl. mAter. Interfaces* **2017**, *9*, 5222–5230. [CrossRef]

45. Samal, S.; Blanco, I. An overview of thermal plasma arc systems for treatment of various wastes in recovery of metals. *Materials* **2022**, *15*, 683. [CrossRef]

46. Kondratowicz, I.; Nadolska, M.; Şahin, S.; Łapiński, M.; Prześniak-Welenc, M.; Sawczak, M.; Sadowskwi, W.; Żelechowska, K. Tailoring properties of reduced graphene oxide by oxygen plasma treatment. *Appl. Surf. Sci.* **2018**, *440*, 651–659. [CrossRef]

47. Duan, L.; Zhao, L.; Cong, H.; Zhang, X.; Lü, W.; Xue, C. Plasma Treatment for Nitrogen-Doped 3D Graphene Framework by a Conductive mAtrix with Sulfur for High-Performance Li–S Batteries. *Small* **2019**, *15*, 1804347. [CrossRef]

48. Hummers, W.S.; Offeman, R.E. Preparation of Graphitic Oxide. *J. Am. Chem. Soc.* **1958**, *80*, 1339. [CrossRef]

49. Kim, C.-G.; Jekal, S.; Otgonbayar, Z.; Kim, J.; Ra, Y.-H.; Noh, J.; Oh, W.-C.; Yoon, C.-M. Synthesis of Plasma-Reduced Graphene Oxide/Lithium Titanate Oxide Composite and Its Application as Lithium-Ion Capacitor Anode mAterial. *Batteries* **2024**, *10*, 311. [CrossRef]

50. Yoon, C.-M.; Jang, Y.; Noh, J.; Kim, J.; Lee, K.; Jang, J. Enhanced Electrorheological Performance of Mixed Silica Nanomaterial Geometry. *ACS Appl. mAter. Interface* **2017**, *9*, 36358–36367. [CrossRef]

51. Noh, J.; Hong, S.; Yoon, C.-M.; Lee, S.; Jang, J. Dual external field-responsive polyaniline-coated mAgnetite/silica nanoparticles for smart fluid applications. *Chem. Commun.* **2017**, *53*, 6645–6648. [CrossRef]

52. Stenina, K.; Minakova, P.; Kulova, T.; Yaroslavtsev, A. Electrochemical Properties of LiFePO$_4$ Cathodes: The Effect of Carbon Additives. *Batteries* **2022**, *8*, 111. [CrossRef]

53. Rastabi, S.R.; mAmoory, R.S.; Biomquist, N.; Phadatare, M.; Olin, H. Synthesis of a NiMoO$_4$/3D-rGO Nanocomposite via Starch Medium Precipitation Method for Supercapacitor Performance. *Batteries* **2020**, *6*, 5. [CrossRef]

54. Zou, G.; Chen, K.; Luo, X.; Fu, Q.; Wu, B. Crystal structure, morphology, and electrical properties of aluminum-doped LFP mAterials. *Batteries* **2024**, *30*, 2549–2563. [CrossRef]

55. Stenina, I.; Safikanov, D.; Minakova, P.; Novikova, S.; Kulova, T.; Yaroslavtsev, A. Composite Cathodes Based on Lithium-Iron Phosphate and N-Doped Carbon mAterials. *Batteries* **2022**, *8*, 256. [CrossRef]

56. Zhu, X.; Hu, J.; Wu, W.; Zeng, W.; Dai, H.; Du, Y.; Liu, Z.; Li, L.; Ji, H.; Zhu, Y. LiFePO$_4$/reduced graphene oxide hybrid cathode for lithium ion battery with outstanding rate performance. *J. mAter. Chem. A* **2024**, *2*, 7812–7818. [CrossRef]

57. Longoni, G.; Panda, J.K.; Gagliani, L.; Brescia, R.; mAnna, L.; Bonaccorso, F.; Pellegrini, V. In situ LiFePO$_4$ nano-particles grown on few-layer graphene flakes as high-power cathode nanohybrids for lithium-ion batteries. *Nano Energy* **2018**, *51*, 656–667. [CrossRef]

58. Kim, J.; Lee, G.; Lee, K.; Yu, H.; Lee, J.W.; Yoon, C.-M.; Kim, S.G.; Kim, S.K. Fluorine plasma treatment on carbon-based perovskite solar cells for rapid moisture protection layer formation and performance enhancement. *Chem. Commun.* **2020**, *56*, 535–538. [CrossRef]

59. Wunderlich, P.; Küpper, J.; Simon, U. Optimizing Discharge Capacity of Graphite Nanosheet Electrodes for Lithium–Oxygen Batteries. *Batteries* **2020**, *6*, 36. [CrossRef]

60. Zhou, S.; Du, J.; Xiong, X.; Liu, L.; Wang, J.; Fu, L.; Ye, J.; Chen, Y.; Wu, Y. Direct recovery of scrapped LiFePO$_4$ by a green and low-cost electrochemical re-lithiation method. *Green Chem.* **2022**, *24*, 6278–6286. [CrossRef]

61. Zhang, W.; Zhan, Y.; Gao, X.; Li, R.; Zhu, W.; Xu, H.; Liu, B.; Fang, X.; Xu, Y.; Ding, T. Effect of oxygen functionalities of graphene oxide on polymerization and thermal properties of reactive benzoxazine nanocomposites. *Macromol. Res.* **2017**, *26*, 77–84. [CrossRef]

62. Tamang, S.; Rai, S.; Bhujel, R.; Bhattacharyya, N.K.; Swain, B.P.; Biswas, J. A concise review on GO, rGO and metal oxide/rGO composites: Fabrication and their supercapacitor and catalytic applications. *J. Alloys Compd.* **2023**, *947*, 169588. [CrossRef]

63. Johra, F.T.; Jung, W.-G. RGO–TiO$_2$–ZnO composites: Synthesis, characterization, and application to photocatalysis. *Appl. Catal. A-Gen.* **2015**, *491*, 52–57. [CrossRef]

64. Gnanamoorthy, G.; Yadav, V.K.; Latha, D.; Karthikeyan, V.; Narayanan, V. Enhanced photocatalytic performance of ZnSnO$_3$/rGO nanocomposite. *Chem. Phys. Lett.* **2020**, *739*, 137050. [CrossRef]

65. Zhou, D.; Qiu, X.; Liang, F.; Cao, S.; Yao, Y.; Huang, X.; mA, W.; Yang, B.; Dai, Y. Comparison of the effects of FePO$_4$ and FePO$_4$·2H$_2$O as precursors on the electrochemical performances of LiFePO$_4$/C. *Ceram. Int.* **2017**, *43*, 13254–13263. [CrossRef]

66. Ke, X.; Xiao, R.-G.; Liao, X.; mA, Z.-M.; Wang, S.-D.; Xu, D. LiFePO$_4$/C cathode mAterial prepared with sphere mesoporous-FePO$_4$ as precursors for lithium-ion batteries. *J. Electroanal. Chem.* **2018**, *820*, 18–23. [CrossRef]

67. Apachitei, G.; Hidalgo, M.; Dogaru, D.; Lain, M.; Heymer, R.; mArco, J.; Copley, M. Optimisation of Industrially Relevant Electrode Formulations for LFP Cathodes in Lithium Ion Cells. *Batteries* **2023**, *9*, 192. [CrossRef]

68. Yoon, C.-M.; Jekal, S.; Kim, D.-H.; Noh, J.; Kim, J.; Kim, H.-Y.; Kim, C.-G.; Chu, Y.-R.; Oh, W.-C. 3D Hierarchically Structured Tin Oxide and Iron Oxide-Embedded Carbon Nanofiber with Outermost Polypyrrole Layer for High-Performance Asymmetric Supercapacitor. *Nanomaterials* **2023**, *13*, 1614. [CrossRef]

69. Seidl, C.; Thieme, S.; Frey, M.; Nikolowski, K.; Michaelis, A. Comparison of Electronic Resistance Measurement Methods and Influencing Parameters for LMFP and High-Nickel NCM Cathodes. *Batteries* **2024**, *10*, 105. [CrossRef]

70. Kim, D.-H.; Jekal, S.; Kim, C.-G.; Chu, Y.-R.; Noh, J.; Kim, M.S.; Lee, N.; Song, W.-J.; Yoon, C.-M. Facile Enhancement of Electrochemical Performance of Solid-State Supercapacitor via Atmospheric Plasma Treatment on PVA-Based Gel-Polymer Electrolyte. *Gels* **2023**, *9*, 351. [CrossRef]

71. Yoon, J.H.; Cho, W.-J.; Kang, T.H.; Lee, M.; Yi, G.-R. Nanostructured Polymer Electrolytes for Lithium-Ion Batteries. *Macromol. Res.* **2021**, *29*, 509–518. [CrossRef]

72. Huang, Y.; Liu, H.; Lu, Y.C.; Hou, Y.; Li, Q. Electrophoretic lithium iron phosphate/reduced graphene oxide composite for lithium ion battery cathode application. *J. Power Sources* **2015**, *284*, 236–244. [CrossRef]

73. Ha, S.H.; Lee, Y.J. Core-Shell LiFePO$_4$/carbon-coated reduced graphene oxide hybrids for high-power lithium-ion battery cathodes. *Chem.–A Eur. J.* **2015**, *21*, 2132–2138. [CrossRef] [PubMed]

74. Mwizerwa, J.P.; Liu, C.; Xu, K.; Zhao, N.; Li, Y.; Ndagijimana, P.; Chen, Z.; Shen, J. Activated carbon/reduced graphene oxide wrapped LiFePO$_4$ cathode for Li-ion batteries with ultrahigh capacities and high specific energy density. *FlatChem* **2022**, *34*, 100393. [CrossRef]

75. Lee, Y.-S.; Ryu, K.-S. Study of the lithium diffusion properties and high rate performance of TiNb$_6$O$_{17}$ as an anode in lithium secondary battery. *Sci. Rep.* **2017**, *7*, 16617. [CrossRef]

76. Shaji, N.; Jiang, F.; Sung, J.Y.; Nanthagopal, M.; Kim, T.; Jeong, B.J.; Jung, S.P.; Lee, C.W. Heteroatoms-doped carbon effect on LiFePO$_4$ cathode for Li-ion batteries. *J. Energy Storage* **2023**, *72*, 108710. [CrossRef]

77. Dong, G.H.; mAo, Y.Q.; Li, Y.Q.; Huang, P.; Fu, S.Y. MXene-carbon nanotubes-Cellulose-LiFePO$_4$ based self-supporting cathode with ultrahigh-area-capacity for lithium-ion batteries. *Electrochim. Acta* **2022**, *420*, 140464. [CrossRef]

78. Xia, Z.; Li, Z.; Xu, J.; Sasidharan, S.; Sanchez, J.S.; Palermo, V.; Asp, L.E. Green synthesis of positive electrodes for high performance structural batteries-A study on graphene additives. *Compos. Sci. Technol.* **2024**, *251*, 110568. [CrossRef]

79. Guo, F.; Kong, Z.; Wang, T.; Liu, X.; Xu, Z.; Fu, A.; Li, Y.; Guo, P.; Guo, Y.G.; Li, H. Porous microspheres consisting of carbon-modified LiFePO$_4$ grains prepared by a spray-drying assisted approach using cellulose as carbon source. *Ionics* **2020**, *26*, 2737–2746. [CrossRef]

80. Liu, X.; Zhao, R.; Xia, Y.; Li, Q. Improved electrochemical performance of LiFePO$_4$/carbon cathode for lithium-ion batteries. *Ionics* **2022**, *28*, 4579–4585. [CrossRef]